Optimized Design Considering the Mass Influence of an Axial Flux Permanent-Magnet Synchronous Generator With Concentrated Pole Windings

Hendrik Vansompel[1], Peter Sergeant[1,2], and Luc Dupré[1]

[1]Department of Electrical Energy, Systems & Automation, Ghent University, B-9000 Ghent, Belgium
[2]Department of Electrotechnology, Faculty of Applied Engineering Sciences, University College Ghent, B-9000 Ghent, Belgium

In this paper, the efficiency optimization of an axial flux permanent-magnet synchronous generator with concentrated pole windings is examined for a 3.6 kW/2000 rpm combined heat and power application. Because the efficiency of the machine is important, specific measures are taken in order to reduce losses in the machine: thin laminated grain oriented material in the teeth, concentrated pole windings, and segmented magnets. A study of the influence of a limited set of geometry parameters on the efficiency of this type of machine is done, using both analytical and finite-element methods. In the analytical as well as in the finite-element model, the inherent 3-D geometry of the axial flux machine is approximated by multiple 2-D models at different radii in circumferential direction. Afterwards, the influence of mass on the optimal values of the geometry parameters and the efficiency is considered, and it is found that mass can be seriously decreased with only a small reduction in efficiency. Finally, the results of both methods are compared with measurements on a prototype to evaluate their validity.

Index Terms—Axial flux machine, efficiency, finite-element methods, optimization, permanent-magnet generators, sustainable energy.

I. INTRODUCTION

THANKS to the high torque output at low speeds, the axial flux permanent-magnet synchronous machine (AF-PMSM) is very suitable for, e.g., wheel motors [1] and direct drive wind energy applications [2]. AFPMSMs exist in different topologies and geometries, each having their advantages and disadvantages. The AFPMSM discussed in this paper is a single-stator double-rotor type with concentrated pole windings [3] (Fig. 1). Concentrated pole windings are preferable to distributed pole windings because of the ease in construction and the short coil ends. The short coil ends allow to reduce the power losses in the copper windings.

Although the nominal speed is 2000 rpm, a machine with 16 poles is chosen, leading to a rated frequency of 267 Hz. To avoid high iron losses in the stator teeth, thin laminated grain-oriented (GO) magnetic material is used. GO-material has the advantage over nonoriented (NO) material, because of the better magnetic characteristics when the flux direction in the major part of the teeth has only an axial component [4].

Although a multiphase system for concentrated pole windings is proposed in [5], a regular three-phase system is used in this paper. In order to obtain a high winding factor, the number of teeth is set to 15 resulting in a winding factor of 0.951 for the 16-pole machine [6].

In [7], the stator teeth are constructed by a single iron strip that is wound in a spiral construction. However, in the present paper each tooth is made separately and the winding is added before placing the tooth into the machine stator. This modular approach has many advantages, i.e., easy to fit winding, each tooth can be easily replaced, etc. The construction of the tooth itself is not
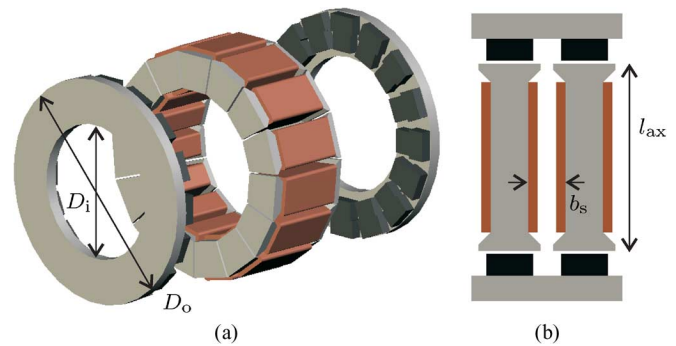
Fig. 1. Topology of the PMSM showing the parameters to optimize. (a) Overview. (b) Detailed view of a tooth pitch.
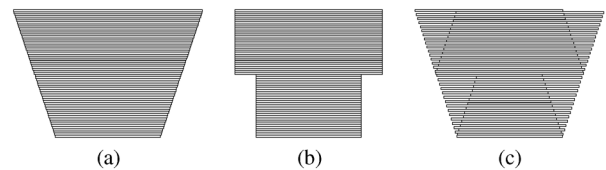

Fig. 2. Different stack configurations of the laminations: (a) ideal full overlap, (b) full overlap with two different lamination types, and (c) alternated with two different lamination types resulting in zones with only partial overlap.

an obvious case. Theoretically each lamination has a different geometry [Fig. 2(a)], which makes the lamination production complicated and expensive. Therefore, in this paper it is chosen to work only with two different lamination geometries that are stacked as shown in Fig. 2(c). This stack configuration has the advantage over Fig. 2(b) that the theoretical 3-D geometry is better approximated.

In [8], the losses in the rotor discs, caused by the stator magnetomotive force (MMF) harmonics, are reduced by using soft magnetic composite (SMC) instead of solid construction steel. As the magnets are closer to the air gap than the rotor discs, the rotor loss is reduced by segmenting the magnets rather than by using SMC. Therefore, the rotor discs in this paper are made of 8

mm thick solid construction steel on which the 16 T-shaped segmented magnets are glued. The magnets from Vacuumschmelze have a remanence of 1.26 T and are segmented in order to reduce eddy-current losses.

So far, thin laminated grain-oriented material in the teeth, concentrated pole windings, segmented magnets, and a high winding factor were introduced to improve the efficiency of the AFPMSG. In this paper, however, the influence of a limited set of four parameters which define the global design of the AFPMSG, is studied. Three of these four parameters are related to the global dimensions of the AFPMSG and are thus related to the mass of the AFPMSG. Actually, active mass should be used instead of mass, because only the masses of materials that participate in the energy conversion are included, i.e., mass of magnetic material, mass of copper windings, and the magnet mass. Masses related to the mechanical structure are thus not included here. However, an increase of active mass requires a more robust mechanical construction and thus the mass of the entire machine will increase. The materials of teeth, magnets, rotor back-iron, and windings are fixed during the optimization, making the material cost proportional to the masses of these materials. The material cost is not taken into account in the optimization. However, as the material cost is proportional to the masses of the active materials, less active mass will result in a lower material cost.

The goal of this research is to investigate the mass influence on the efficiency of the AFPMSG. The study of cogging torque and torque ripple, which is the object of much recent research [9]–[11], has not been extensively examined in this paper. However, due to the combination of 16 magnets and 15 stator teeth, the machine has no symmetry and therefore the cogging torque and torque ripple are expected to have a small period and amplitude.

II. ANALYTICAL AND FINITE-ELEMENT MODEL

Despite the inherent 3-D geometry of the AFPMSG, analytical models as well as FEM are very often 2-D models taken at the average diameter. Although the computation time is low compared to 3-D FEM, these models are often not accurate enough. A compromise between both computation time and accuracy is found in [12] and [13] where a "quasi 3-D" approximation is proposed. This "quasi 3-D" approximation defines multiple 2-D models at different radii in circumferential direction. Afterwards, the global solution is found by a weighted summation of the contribution of each computation plane (CP). The number of computation planes is again a tradeoff between calculation time and accuracy. Due to the many evaluations in the optimization procedure, only two computation planes with equal thickness are used in the preliminary design [Fig. 3(a)]. Once the optimization is performed, a more accurate approximation of the selected geometry is performed using six computation planes with unequal thickness [Fig. 3(b)]. In order to take the T-shaped magnet and the lamination stack configuration into account, at least two CPs are necessary. Experimentally, it was found that 6 CPs with nonequal thickness are enough to achieve sufficiently accurate simulation results.

A. Analytical Model

An analytical model of the air-gap flux density distribution allows the calculation of important design parameters like the
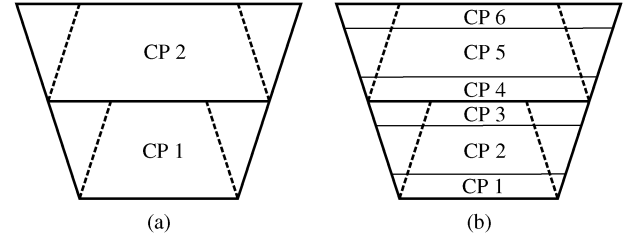

Fig. 3. Sectioning of the 3-D in geometry into the different computation planes (CP): (a) used in the optimization, and (b) used in simulations.
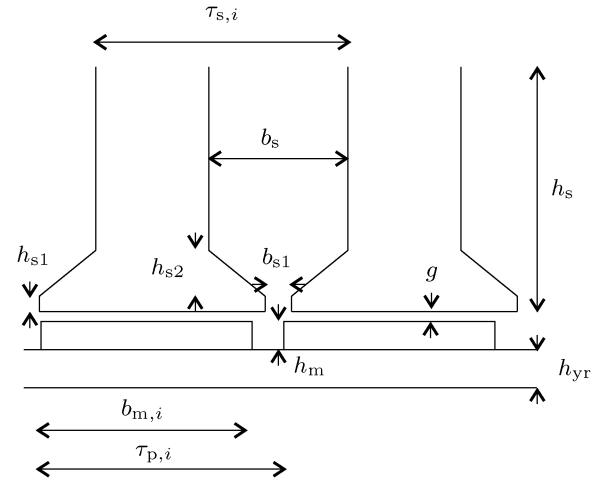

Fig. 4. Geometry parameters of the AFPMSG in a CP.

electromotive force (EMF) and cogging torque. The air-gap flux density distribution can be expressed as

$$B_{\mathrm{ag},i}(x) = \tilde{\lambda}_i(x) B_i(x) \tag{1}$$

where $B_i(x)$ is the flux distribution in the ith CP caused by the permanent magnets calculated by (2) which is proposed in [14]

$$B_i(x) =$$

$$-\sum_{n=1,3,5,\ldots}^{\infty} \frac{\frac{8B_r}{n\pi}\sin\left(\frac{\alpha_{\mathrm{p},i}n\pi}{2}\right)e^{-\frac{n\pi g'_i}{\tau_{\mathrm{p},i}}}\cos\left(\frac{n\pi x}{\tau_{\mathrm{p},i}}\right)}{\left(e^{-\frac{2n\pi g'_i}{\tau_{\mathrm{p},i}}}+1\right)+\frac{\mu_{\mathrm{m}}\left(-e^{-\frac{2n\pi g'_i}{\tau_{\mathrm{p},i}}}+1\right)\left(e^{-\frac{2n\pi h_{\mathrm{m}}}{\tau_{\mathrm{p},i}}}+1\right)}{\left(e^{-\frac{2n\pi h_{\mathrm{m}}}{\tau_{\mathrm{p},i}}}-1\right)}} \cdot \tag{2}$$

In these equations, Q_s is the number of slots, B_r the remanent flux density of the permanent magnets, and $\alpha_{\mathrm{p},i}$ is the ratio between the magnet width $b_{\mathrm{m},i}$ and the pole pitch $\tau_{\mathrm{p},i}$. All other parameters are defined in Fig. 4.

The effect of the slot openings is modeled by the relative permeance function $\tilde{\lambda}_i(x)$ introduced in [15] given by

$$\tilde{\lambda}_i(x) = \frac{\lambda_i}{\frac{\mu_0}{g+h_{\mathrm{m}}/\mu_{\mathrm{m}}}} \tag{3}$$
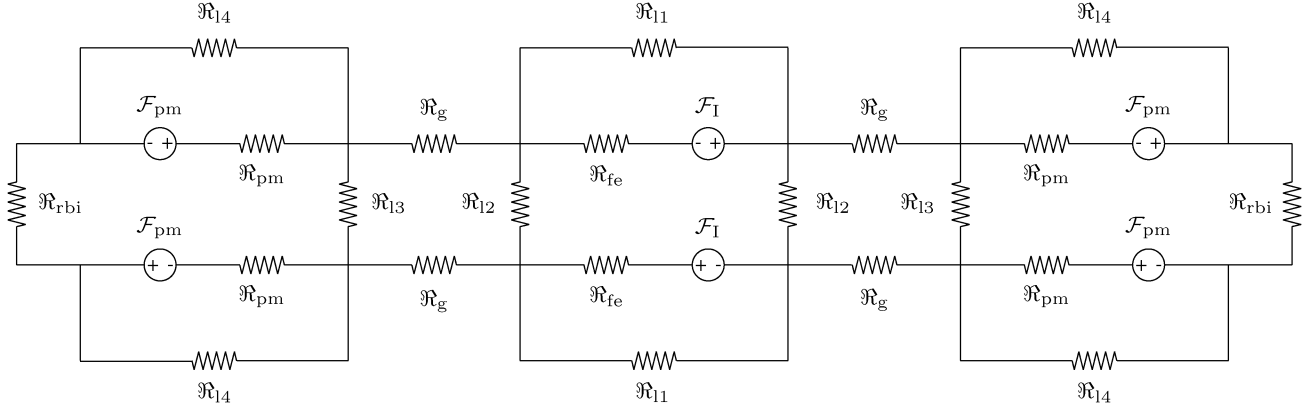
Fig. 5. Simple reluctance network of the dual-rotor single-stator AFPMSG with concentrated pole windings. Due to symmetry in the flux pattern, only two teeth and magnets are modeled.

where

$$\lambda_i = \frac{\mu_0}{g + \frac{h_m}{\mu_m} + \frac{2\pi r_{s,i}}{4}} \tag{4}$$

for $(k-1)\tau_{s,i} - b_{s1}/2 \le x \le (k-1)\tau_{s,i} + b_{s1}/2$, where $k = 1, 2, \ldots, Q_s$.

Based on (1), the induced no-load electromotive force (EMF) e_{ij} in one winding of tooth j in the ith CP can be calculated as

$$e_{ij}(t) = -\frac{\partial}{\partial t} \left(\int_{(j-1)\tau_{s,i}}^{j\tau_{s,i}} \int_0^{h_{s,i}} B_{ag,i}(x) \mathrm{d}x \mathrm{d}h \right) \tag{5}$$

where $\tau_{s,i}$ is the tooth pitch and $h_{s,i}$ is the thickness of the computation plane. The total EMF induced in one turn of phase a can be calculated by

$$e_a(t) = \sum_i \sum_{j=1}^N e_{ij}(t). \tag{6}$$

The sum is taken over all the CPs and for all N teeth in a phase. Note that the amplitude of (6) is less that the sum of the amplitudes of the individual teeth due to the phase difference of the induced EMF in the different teeth. Thanks to the good combination of magnets and teeth, i.e., respectively 16 and 15, the winding factor is 0.951.

Based on the rms value of (6) and the desired rms phase voltage V_{ph} at nominal speed, the number of turns per tooth can be calculated. Out of the nominal electric power output P and the phase voltage V_{ph}, the rms phase current I_{ph} can be calculated.

In both the analytical and finite-element model, the efficiency η is expressed by

$$\eta = \frac{P}{P + P_{fe} + P_{cu} + P_m} \tag{7}$$

where P_{fe}, P_{cu}, and P_m represent the iron, copper, and mechanical losses, respectively. The mechanical losses are not taken into account in the analytical and finite-element model.

The copper losses are calculated using the phase resistance R_{ph} and the phase current I_{ph}. The iron losses are calculated

by the improved iron loss equations [16] which divides the iron losses into a hysteresis, a classical, and an excess loss component

$$P_{fe} = k_h f B_p^\alpha + k_e f^2 B_p^2 + k_{exc} f^{1.5} B_p^{1.5}. \tag{8}$$

This equation requires the peak flux density B_p in the teeth, which is determined using a simple nonlinear reluctance network (Fig. 5), similar to the one used in [17]. This network contains the slot leakage reluctance $\Re_{l1}$, the magnet leakage reluctance $\Re_{l4}$, the leakage flux reluctance between two teeth-tips $\Re_{l2}$, the leakage flux reluctance between two magnets $\Re_{l3}$, the reluctance of the rotor back-iron $\Re_{rbi}$, the reluctance of the permanent magnets $\Re_{pm}$ and the reluctance of the teeth in GO-material $\Re_{fe}$.

For the elements of the reluctance network that represent the elements of the teeth, the relative permeability μ_r of the GO-material in the rolling direction is used. As μ_r is a function of B_p, the reluctance elements $\Re_{fe}$ corresponding with the GO-material are defined by

$$\Re_{fe} = \frac{l_{fe}}{\mu_0 \mu_r(B_p) S_{fe}}. \tag{9}$$

Next to the MMF-source $\mathcal{F}_{pm}$ that models the permanent magnets, an extra MMF-source $\mathcal{F}_I$ is added to the reluctance network to model the influence of stator currents on the saturation in the teeth. By introducing the material characteristic in the stator teeth reluctance, solving the nonlinear reluctance network is done iteratively. Notice that a reluctance network is built for each CP.

In spite of the filling factor in the zones with partial overlap (Fig. 6) being only 50%, the analytical model uses a filling factor of 100% and thus follows the theoretical 3D geometry (Fig. 2(a)).

B. Finite Element Model

Unlike the analytical model, the FEM does model the zones with partial overlap. Different material properties are given to the full-overlap zone and the partial-overlap zone (Fig. 6).

The material model for the GO-material in the teeth is an anisotropic model based on the magnetic energy presented in [4] as a variant on [18]. The anisotropic model returns the mag-
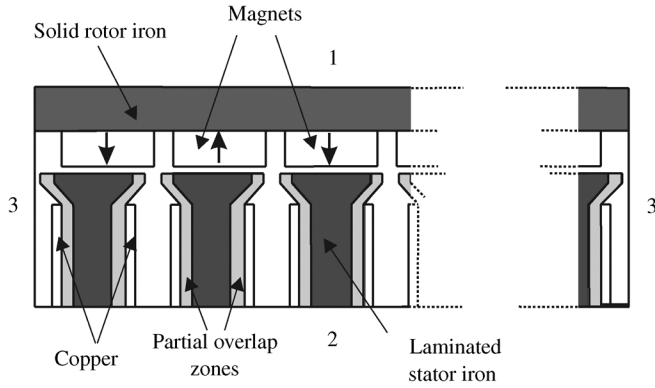
Fig. 6. Schematic representation of a 2D computation plane containing 15 teeth and 16 magnets; teeth are divided in a zone with full overlap and two zones with only partial overlap. 1 Dirichlet boundary condition, 2 Neumann boundary condition, 3 periodic boundary condition.

netization vector $\mathbf{M}$ as a function of an induction vector $\mathbf{B}$. The equation for the magnetic potential $\mathbf{A}$ equals

$$\nabla \times \left(\frac{1}{\mu_0} \nabla \times \mathbf{A} \right) - \nabla \times \mathbf{M} = \mathbf{J}_e \qquad (10)$$

where $\mathbf{J}_e$ is the external current density. As said before, the anisotropic model is based on the magnetic energy

$$W_{em}(\mathbf{B}) = \int_0^{\mathbf{B}} \mathbf{H}(\mathbf{B}) \cdot d\mathbf{B}. \qquad (11)$$

When losses are absent, the gradient of this energy function gives the magnetic field

$$\mathbf{H}(\mathbf{B}) = \nabla_B W_{em}(\mathbf{B}) = \frac{\partial W_{em}(\mathbf{B})}{\partial B_x} \mathbf{1}_x + \frac{\partial W_{em}(\mathbf{B})}{\partial B_y} \mathbf{1}_y. \qquad (12)$$

The magnetization vector used in (10) can be calculated as

$$\mathbf{M}(\mathbf{B}) = \nu_0 \mathbf{B} - \mathbf{H}(\mathbf{B}). \qquad (13)$$

Calculation of the iron losses is done *a posteriori*, based on the simulated field waveforms. Therefore, the B_x and B_y are determined in multiple points in the stator tooth. By analyzing the simulated field waveforms it is observed that no minor loops are present, and that the field is only nonunidirectional in small parts of the tooth. However, in the small parts where the field is nonunidirectional, a dominant direction can be detected.

Calculation of the iron losses is separated into a hysteresis, a classical and an excess loss component [19], [20]. While minor loops are absent, the hysteresis loss is determined by the peak value of the induction. Hysteresis losses are determined using a 2D lookup table containing the hysteresis loss for several peak values and directions. Losses are quantified as the losses corresponding with a unidirectional waveform along the dominant direction. The waveform is obtained by projecting the $\mathbf{H}$-vector on the dominant direction.

The classical energy loss per cycle depends on the time derivative of $B(t)$

$$W_{cl} = \frac{1}{12} \sigma d^2 \int_0^T \left(\frac{dB}{dt} \right)^2 dt \qquad (14)$$
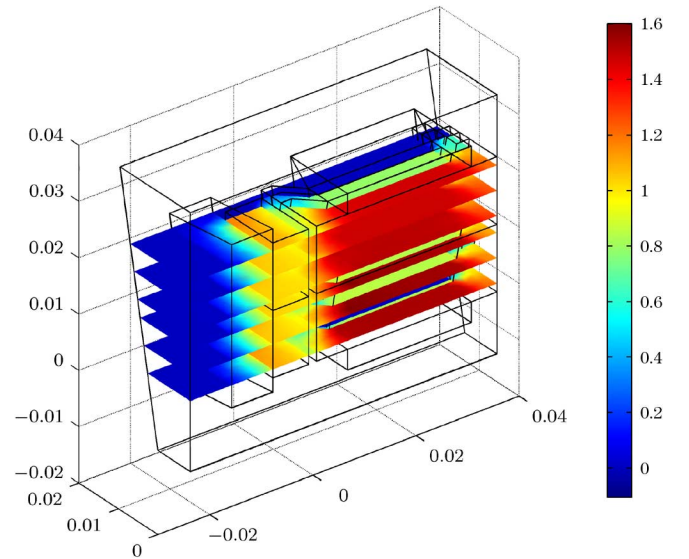

Fig. 7. Slice plot of the axial component of the magnetic flux density. Each slice plot is located at the same radius as a computation plane in the "quasi 3D"-FEM. Magnet aligned with tooth and zero current imposed.

where σ is the conductivity and d the lamination thickness.

The instantaneous excess power loss $p_{exc}(t)$ is given by

$$p_{exc}(t) = \frac{n_o V_o}{2} \left(\sqrt{1 + \frac{4\sigma G S}{n_o^2 V_o} \left| \frac{dB}{dt} \right|} - 1 \right) \left| \frac{dB}{dt} \right|. \qquad (15)$$

In this equation, n_o is the number of simultaneously active magnetic objects for frequency $f \to 0$ and V_o defines the statistics of the magnetic objects. The dimensionless coefficient $G = 0.1356$ and the lamination cross section S are known constants. Notice that in the losses (8) of the analytical model, the excess loss is simplified to a "high frequency" approximation of (15):

$$p_{exc}(t) = \sqrt{\sigma G S V_o} \left| \frac{dB}{dt} \right|^{\frac{3}{2}}. \qquad (16)$$

The parameters that define the anisotropic material model and the loss model are fitted from different measurements performed using an Epstein frame. Therefore, strips in seven different directions, $0°$, $15°$, $30°$, $45°$, $60°$, $75°$, and $90°$, are cut from a sheet of GO-material and measurements are done with several frequencies and amplitudes for the magnetic field.

A similar procedure as described in the analytical model is followed, but now EMF and iron losses are calculated based on "quasi 3D"-FEM simulations. The iron losses predicted by FEM are evaluated in multiple points in the tooth while the improved iron loss (8) in the analytical model calculates the iron losses as a global quantity based on the average peak flux density in the teeth. Therefore, the iron losses based on FEM are much more accurate than the analytical ones.

Despite the different calculation method, the iron losses in the analytical and "quasi 3D"-FEM are calculated for each individual CP. This approach is only valid if the flux densities in the different CP's correspond to the flux densities in the same planes in a full 3D model. Therefore, a 3D-model of a half tooth aligned with a half magnet is built (Fig. 7). This model takes

TABLE I
AXIAL COMPONENT OF THE FLUX DENSITY IN THE CENTER PART OF A TOOTH
FOR THE DIFFERENT COMPUTATION PLANES WHEN A MAGNET IS ALIGNED.
VALUES TAKEN IN THE ZONES WITH 100% FILLING FACTOR

CP #	Analytical	"quasi 3D" FEM	3D FEM
1	1.7434	1.4835	1.5101
2	1.6246	1.5357	1.5199
3	1.5356	1.5460	1.5097
4	1.4734	1.4378	1.4847
5	1.4169	1.4404	1.4709
6	1.3679	1.4728	1.4634

TABLE II
OPTIMIZED PARAMETER VALUES OBTAINED WITH ANALYTICAL AND FEM
MODEL AND EFFICIENCY η

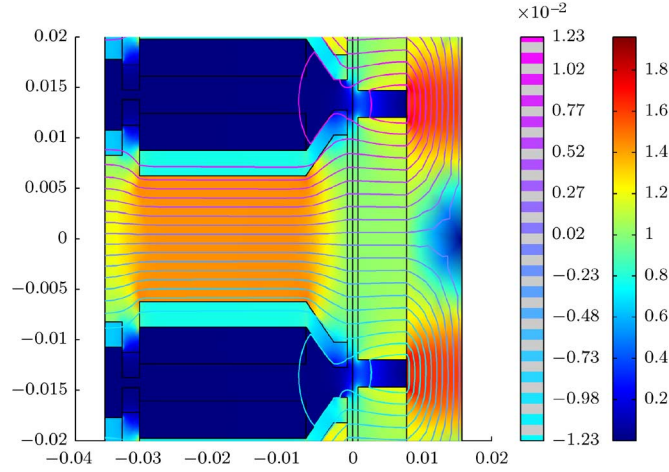| Parameter	Range	Analytical	"quasi 3D" FEM
D_o [mm]	50-150	150	150
D_i [mm]	50-150	89.7	82.1
l_ax [mm]	10-100	78.6	82.2
b_s [mm]	3-15	8.1	5.7
η [%]	-	97.09	97.22

Fig. 8. Detail view of computation plane 5 of the "quasi 3D"-FEM: zones with full- and partial overlap are given different material properties. Contour plot: magnetic potential, surface plot: magnetic flux density. Magnet aligned with tooth and zero current imposed.

the effect of the lamination in the radial direction into account, which cannot be modeled in the "quasi 3D"-FEM.

A magnet aligned with a tooth results in the highest flux through the tooth, and thus the highest flux density values and may saturate the tooth-iron. The flux densities of the different slices (Fig. 7) are then compared with data obtained from the corresponding CP (Fig. 8). As the analytical model uses only the peak flux density, in Table I the peak flux densities in the analytical model are compared with these found in the center part of the teeth in the "quasi 3D"-FEM and 3D-FEM. Table I shows a good correspondence between the three data sets. As the values in the "quasi 3D"-FEM and 3D-FEM are almost equal, a loss calculation based on the "quasi 3D"-FEM can be done without making a significant error.

III. OPTIMIZATION

The objective of the optimization is to maximize the efficiency of the AFPMSG at rated speed and load, i.e., 2000 rpm and 3.6 kW. Despite the large number of parameters that determine the AFPMSG, the influence of only 4 basic parameters is studied (Fig. 1): 3 parameters which define the global geometry, i.e., the outer diameter D_o, the inner diameter D_i and the axial length of the teeth l_ax and one parameter that specifies the ratio copper to iron section: the slot width in the center section b_s. All other parameters are fixed during the optimization because their influence on the global machine geometry is less important.

For the analytic optimization, a genetic algorithm (GA) is used to ensure that a global optimum is found. Afterwards a constrained nonlinear optimization algorithm using FEM is applied. The optimized values of the analytic optimization are hereby used as initial values. The line of thought to this approach is that a rapid optimization based on the analytical model is possible, while the number of evaluations to reach convergence using the FEM model is seriously reduced because the starting parameter values are close to the optimal ones.

The values obtained in both simulations are presented in Table II. Restrictions on the outer diameter result in a parameter value D_o that sticks at the upper boundary. Limitation of the outer diameter is often necessary for integration of the AFPMSG in a construction.

The active mass of this optimized geometry is 8.77 kg. With this mass as a reference, the influence of the mass on the 4 geometry parameters and the efficiency is now investigated. Therefore, mass is varied from 0.3 to 1.5 times the reference mass in steps of 0.05 and an optimization based on a GA using the analytical model is performed again. As mass is an independent variable, one of the 4 geometry parameters is expressed as a function of mass and the other 3 geometry parameters.

In Fig. 9(a) the optimized efficiency values are shown as a function of mass. This curve is very flat around the point of maximal efficiency, this means that changes in mass in this region have only a minor influence on the generators efficiency. In Fig. 9(b), the copper and iron losses are shown as a function of mass. It is clear that, even at a speed of 2000 rpm, the iron losses in the AFMPSG with 8 pole pairs are still quite low: only 30 W for the AFPSG with 1 p.u. mass. Moreover it is found that the optimized values for the flux density are near the saturation value. This allows the teeth section to be smaller, and thus the copper section to be larger which is advantageous for the copper losses.

In Fig. 9(c) the geometry parameters are set as a function of mass. The outer diameter D_o is only lower than the upper boundary for very low values of the active mass. A decrease of the inner diameter D_i results in an increase of the physical flux, and thus less turns are required. Using less turns results in a larger wire diameter and thus less copper losses but higher iron losses because of the increasing iron mass. An increase in the axial length results in a larger copper section and thus lower copper losses, but a higher iron mass and thus higher iron losses. The slot width in the center section b_s, which is an indication of the copper to iron section, shows that with increasing mass, a smaller copper to iron section is proposed.

When mass exceeds the reference mass, due to the limitation on the outer diameter, copper and iron are added in places where
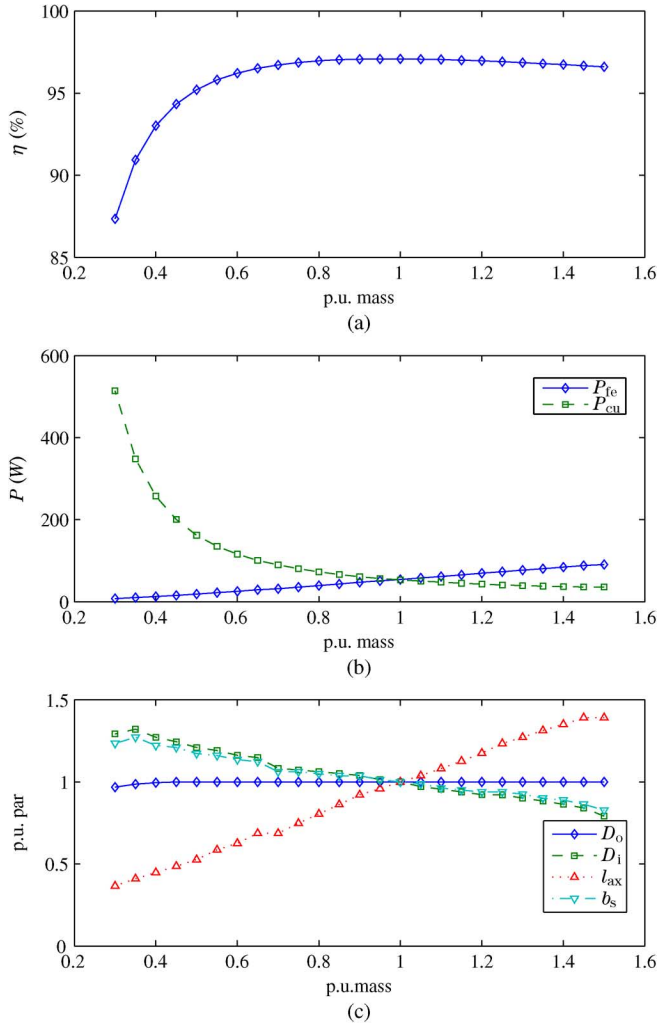
Fig. 9. Influence of mass variation; (a) on the efficiency, (b) on the copper and iron losses, (c) on the 4 basic parameters.
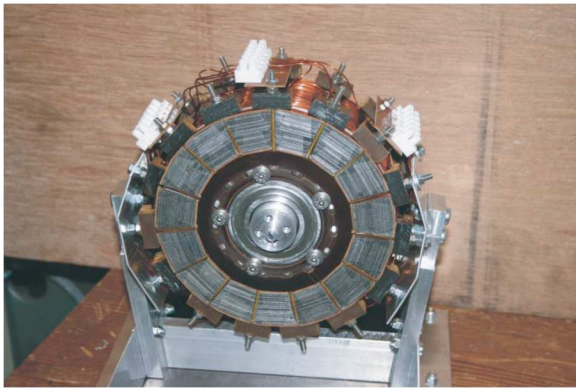

Fig. 10. Photo of the stator of the AFPMSG prototype. The 3 terminals allow measurements on each individual tooth.

the power conversion is less effective, resulting in a decrease of the generators efficiency.

TABLE III
CHARACTERISTICS AND PARAMETERS OF THE BUILT AFPMSG PROTOTYPE. GEOMETRIC PARAMETERS ARE ASSIGNED ACCORDING TO FIG. 4

Parameter	Symbol	Value
Electrical output power (W)	P	3600
Rated speed (rpm)	N_m	2000
Rated torque (Nm)	T	17.2
Rms phase voltage (V)	V_{ph}	180
Rms phase current (A)	I_{ph}	6.67
Phase resistance (Ω)	R_{ph}	2.02
Phase inductance (mH)	L_{ph}	11.3
Magnet width (mm)	b_m	18/24
Magnet height (mm)	h_m	7
Rotor backiron thickness (mm)	h_{yr}	8
Airgap length (mm)	g	1.5
Tooth-tip opening (mm)	b_{s1}	3
Tooth-tip lenght (mm)	h_{s1}	2
Tooth-tip slope length (mm)	h_{s2}	4

IV. SIMULATIONS AND MEASUREMENTS

A. Experimental Setup

Once the optimization process is finished, a prototype of the proposed machine is built (Fig. 10, Table III). Because of the flat mass-efficiency curve near the point of maximal efficiency, it was chosen to built a AFPMSG with less mass. Therefore, D_o was set to 148 mm, D_i to 100 mm, l_{ax} to 60 mm and b_s to 11 mm resulting in an active mass of only 6 kg, which is less than 70% of the reference mass. Despite a large value of b_s is selected, the slots are only partially filled with copper for construction reasons.

To perform measurements on the AFPMSG, an experimental setup was built. In this setup the AFPMSG is connected to a 2-pole 7.5 kW induction motor via a torque sensor. This induction motor is fed by a 11 kW inverter that is controlled by Lab-VIEW. An optical position sensor is used to obtain the shaft speed, and a voltage measurement on the terminals of the AF-PMSG is performed. Although each phase consists of 5 teeth, the winding of each individual tooth is accessible. The data retrieved from voltage, torque and speed measurement is sampled by a National Instruments data-acquisition system with a sampling speed up to 250 kSamples/second.

B. Model Verification

Although the construction of each individual tooth including winding is easy, assembling a stator of the different teeth is mechanically difficult to achieve. Due to the imperfect stator construction, alternating stresses occur in the bearings, shaft and torque sensor during rotation. They result in supplementary losses, and therefore the mechanical losses in (7) can no longer be neglected and result in a lower efficiency.

Simulations at rated speed of 2000 rpm and nominal current of 6.67 A of the built prototype with reduced copper section using analytical expressions and FEM predict an efficiency of 94.7% and 94.9% respectively, while measurements on the prototype indicate an efficiency of only 87.8%. Assuming that both models predict the losses, i.e., copper and iron losses (Table IV)

TABLE IV
IRON LOSSES OF THE PROTOTYPE MACHINE CALCULATED BASED ON
ANALYTICAL MODEL AND "QUASI 3D"-FEM

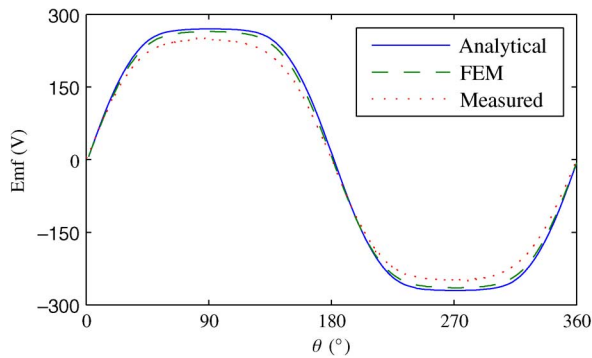| Iron loss	Analytical	"quasi 3D"-FEM
No-load (W)	28.1458	28.2322
Full-load (W)	33.5285	31.4760

Fig. 11. Comparison of the no-load EMF-waveforms at 2000 rpm as a function of the electric angle.

correctly, the mechanical power conversion in the experimental setup has an efficiency of only 92.6%. Although this mechanical power conversion efficiency seems rather low, operation in no-load conditions showed significant local heat production around the bearings while the warming-up of the teeth, magnets and rotor iron was almost imperceptible.

At no-load a measurement of the phase EMF-waveform at 2000 rpm is also done. This waveform is compared with data obtained from simulations using analytical expressions and FEM for the same conditions. The results are presented in Fig. 11. The waveform is similar but the measured waveform has a slightly lower amplitude.

V. CONCLUSION

In this paper, the energy efficiency of an AFPMSM is optimized by using analytical expressions as well as by FEM, studying the influence of 4 basic parameters. First an efficiency optimization without any mass constraints is performed, leading to a most-efficient generator. With the mass of this most-efficient generator as a reference, different masses are imposed and the efficiency optimization is performed repeatedly for each mass. It is shown that the mass-efficiency curve has a flat course near the point of maximum efficiency, which means that mass can be seriously decreased with only a small reduction in efficiency. This reduction in mass can be important for mobile applications and allows a machine construction with lower material costs. The correctness of both analytical and finite element model, on which the optimization procedure is based, are proved by measurements on a prototype.

ACKNOWLEDGMENT

REFERENCES

[1] Y. P. Yang and D. S. Chuang, "Optimal design and control of a wheel motor for electric passenger cars," *IEEE Trans. Magn.*, vol. 43, no. 1, pp. 51–61, Jan. 2007.

[2] M. Andriollo, M. De Bortoli, G. Martinelli, A. Morini, and A. Tortella, "Permanent magnet axial flux disc generator for small wind turbines," in *Proc. 18th Int. Conf. Electrical Machines*, Sep. 6–9, 2008, pp. 1–6.

[3] W. Fei and P. C. K. Luk, "An improved model for the back-EMF and cogging torque characteristics of a novel axial flux permanent magnet synchronous machine with a segmental laminated stator," *IEEE Trans. Magn.*, vol. 45, no. 10, pp. 4609–4612, Oct. 2009.

[4] D. Kowal, P. Sergeant, L. Dupré, and A. Van den Bossche, "Comparison of non-oriented material and grain oriented material for an axial flux permanent-magnet machine," *IEEE Trans. Magn.*, vol. 46, no. 2, pp. 279–285, Feb. 2010.

[5] S. Brisset, D. Vizireanu, and P. Brochet, "Design and optimization of a nine-phase axial-flux PM synchronous generator with concentrated winding for direct-drive wind turbine," *IEEE Trans. Ind. Appl.*, vol. 44, no. 3, pp. 707–715, May–Jun. 2008.

[6] J. Cros and P. Viarouge, "Synthesis of high performance PM motors with concentrated windings," *IEEE Trans. Energy Convers.*, vol. 17, no. 2, pp. 248–253, Jun. 2002.

[7] A. B. Letelier, D. A. Conzalez, J. A. Tapia, R. Wallace, and M. A. Valenzuela, "Cogging torque reduction in an axial flux PM machine via stator slot displacement and skewing," *IEEE Trans. Ind. Appl.*, vol. 43, no. 3, pp. 685–693, May–Jun. 2007.

[8] F. Marignetti, V. D. Colli, and S. Carbone, "Comparison of axial flux PM synchronous machines with different rotor back cores," *IEEE Trans. Magn.*, vol. 46, no. 2, pp. 598–601, Feb. 2010.

[9] P. Virtic, P. Pisek, M. Hadziselimovic, T. Marcic, and B. Stumberger, "Torque analysis of an axial flux permanent magnet synchronous machine by using analytical magnetic field calculation," *IEEE Trans. Magn.*, vol. 45, no. 3, pp. 1036–1039, Mar. 2009.

[10] C.-C. Hwang, P.-L. Li, F. C. Chuang, C.-T. Liu, and K.-H. Huang, "Optimization for reduction of torque ripple in an axial flux permanent magnet machine," *IEEE Trans. Magn.*, vol. 45, no. 3, pp. 1760–1763, Mar. 2009.

[11] J. H. Choi, J. H. Kim, D. H. Kim, and Y. S. Baek, "Design and parametric analysis of axial flux PM motors with minimized cogging torque," *IEEE Trans. Magn.*, vol. 45, no. 6, pp. 2855–2858, Jun. 2009.

[12] R. J. Wang and M. J. Kamper, "Evaluation of eddy current losses in axial flux permanent magnet (AFPM) machine with an ironless stator," in *Conf. Rec. 37th IEEE IAS Annu. Meeting*, Pittsburgh, PA, Oct. 2002.

[13] A. Parviainen, M. Niemelä, and J. Pyrhönen, "Modeling of axial permanent-magnet machines," *IEEE Trans. Ind. Appl.*, vol. 40, no. 5, pp. 1333–1340, Sep.–Oct. 2004.

[14] M. J. Chung and D. G. Gweon, "Modeling of the armature slotting effect in the magnetic field distribution of a linear permanent magnet motor," *Elect. Eng.*, vol. 84, pp. 101–108, 2002.

[15] Z. Q. Zhu and D. Howe, "Analytical prediction of the cogging torque in radial-field permanent magnet brushless motors," *IEEE Trans. Magn.*, vol. 28, no. 2, pp. 1371–1374, Mar. 1992.

[16] F. Deng, "An improved iron loss estimation for permanent magnet brushless machines," *IEEE Trans. Energy Convers.*, vol. 14, no. 4, pp. 1391–1395, Dec. 1999.

[17] M. Sadeghierad, A. Darabi, H. Lesani, and H. Monsef, "Rotor yoke thickness of coreless high-speed axial-flux permanent magnet generator," *IEEE Trans. Magn.*, vol. 45, no. 4, pp. 2032–2037, Apr. 2009.

[18] T. Pera, F. Ossart, and T. Waeckerle, "Field computation in non linear anisotropic sheets using the coenergy model," *IEEE Trans. Magn.*, vol. 29, no. 6, pp. 2425–2427, Nov. 1993.

[19] G. Bertotti, *Hysteresis in Magnetism*. New York: Academic, 1994, p. 401.

[20] E. Barbisio, F. Fiorillo, and C. Ragusa, "Predicting loss in magnetic steels under arbitrary induction waveform and with minor hysteresis loops," *IEEE Trans. Magn.*, vol. 40, no. 4, pp. 1810–1819, Jul. 2004.